

# Proposal for New Hearth Roller Consisting of Ceramic Sleeve and Steel Shafts Used in the Heat Treat Furnace

Nao-Aki NODA,\* Dedi SURYADI, Shintarou MATSUDA, Yoshikazu SANO and Yasushi TAKASE

Mechanical Engineering Department, Kyushu Institute of Technology, 1-1 Sensui-cho, Tobata-ku, Kitakyushu-shi, 804-8550 Japan.

(Received on May 8, 2015; accepted on August 10, 2015)

Conventional rollers used in a heat furnace are called hearth roll. They must be changed very frequently since high temperature of the furnace induces wear on the roll surface in short period. This paper therefore discusses a new roller structure consisting of ceramic sleeve and steel shaft connected by shrink fitting. Although all ceramic sleeve has high temperature resistance and high corrosion resistance, attention should be paid for the risk of fracture due to the thermal expansion of the steel shaft that is much larger than the one of ceramic. Simple double cylinder simulation suggests that thinner structure is useful for reducing thermal stress. The finite element analysis shows that tapered shaft thickness is desirable for the ceramics hearth roller. Finally, an application of ceramic roller to steel manufacturing machinery is considered by changing geometry and material. Since only low shrink fitting ratio can be applied to the new roller, failure analysis is also considered for preventing the coming out of the shaft from the ceramic sleeve.

KEY WORDS: ceramic roller; shrink fitting; fatigue; thermal stress; finite element method.

## 1. Introduction

Advanced structural ceramics have been used since 1970s as electrical insulator, automotive engines,<sup>1,2)</sup> tribology components,<sup>3)</sup> cylinder head plates, pistons and turbocharger rotors, machine tools, hot rolling mills and low-pressure die casting machine. Several marketing researches for the advanced ceramic have been done in USA, Japan, and Germany. Under both thermal and mechanical loadings, however, structural ceramic is not very popular until now compared to functional ceramic widely used.<sup>4)</sup> As an example, intense efforts have been done to develop ceramic gas turbine during 1950s–1990s, but only ceramic coatings are in use now. This is because all ceramic components may be too brittle to design turbine component. Generally speaking, advanced ceramic projects have not progressed very well as shown in this example.

On the other hand, for treatment of molten metal, ceramic die cast sleeves and ceramic stalks in the low-pressure die casting machine are commonly used now.<sup>5–8)</sup> As an extension of those cylindrical components, large ceramic rolls are recently developed for galvanizing steel line, and other applications are being considered.<sup>9)</sup> Since conventional cast iron and stainless steel rolls used in molten metal need high cost of maintenance,<sup>10)</sup> ceramic use may contribute reducing the costs significantly.<sup>11)</sup>

In this study therefore we will focus on hearth rollers used in the heating furnace whose atmosphere temperature is more than 1 000°C as shown in **Fig. 1(a)**. Conventional

rollers have ceramic coated steel sleeve and shafts connected each other by shrink fitting as shown in **Fig. 1(b)**. Although the inside of the roller is cooled by water circulation to reduce the temperature, the roller coating deteriorates in short period due to the thermal expansion difference between ceramic and steel. Then, finally, the conventional rollers are changed very frequently because of the wear induced by the hot conveyed strips.

In previous studies thermal stress was discussed for rolls consisting of ceramic sleeve and ceramic shaft used in molten metal.<sup>12)</sup> Maximum stress for shrink fitting system used for ceramic conveying rollers with steel shaft was considered under room temperature with varying shrink fitting ratio.<sup>13)</sup> Regarding the conventional structure in **Fig. 1(b)** used under high temperature, water cooling system was discussed as well as how to reduce joint stress by inserting buffer layer.<sup>14)</sup> However few references are available for ceramic/steel joints under high temperature without inserting buffer and without water circulation.

In this study therefore a new roller is considered focusing on the joint structure as shown in **Fig. 1(c)**. Then the effects of roller geometry and the material difference will be considered in order to reduce the thermal stress and mechanical stress. Finally, most desirable geometry and materials will be proposed by considering the use at steel manufacturing machinery.

## 2. Small Thickness Structure Can Reduce Thermal Stress

In the previous study [13], the ceramic roller structure was studied at room temperature when a ceramic sleeve

\* Corresponding author: E-mail: noda@mech.kyutech.ac.jp  
DOI: <http://dx.doi.org/10.2355/isijinternational.ISIJINT-2015-246>

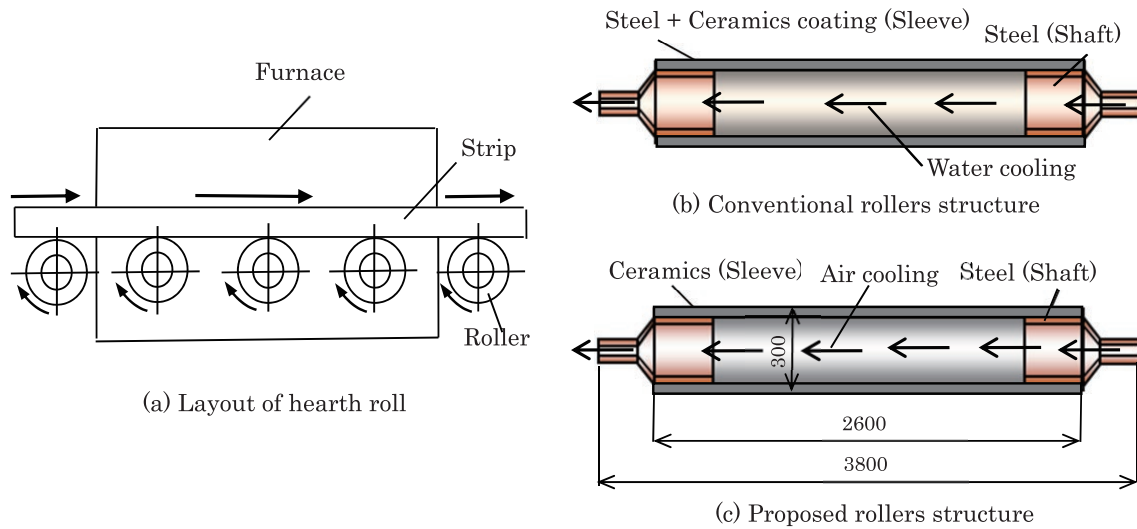


**Fig. 1.** Conventional and proposed rollers for heating furnace (a) Layout of hearth roll, (b) Conventional rollers structure, (c) Proposed rollers structure. (Online version in color.)

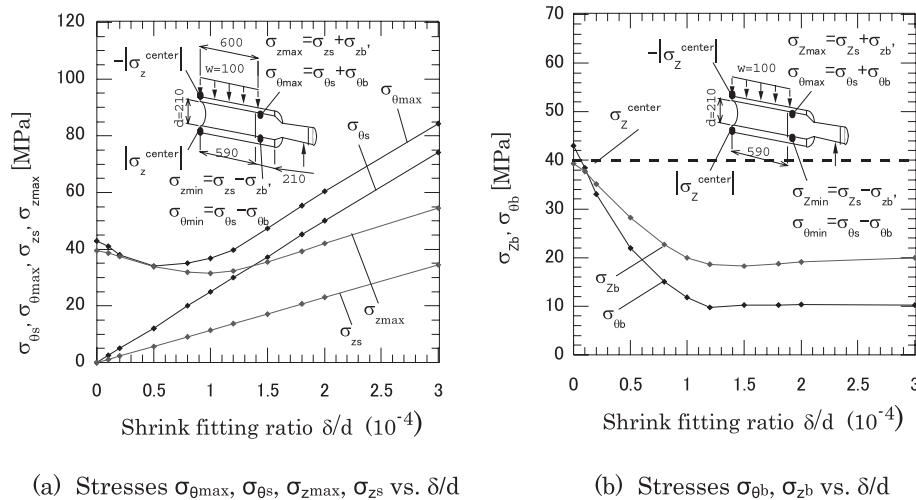


**Fig. 2.**  $\sigma_{\theta}$  vs  $\delta/d$  when  $L=210$  mm (Roll dimensions are different from the ones of Fig. 1). ( $\sigma_{\theta_{max}} = \sigma_{\theta_s} + \sigma_{\theta_b}$ ,  $\sigma_{\theta_s}$  = stress due to shrink fitting,  $\sigma_{\theta_b}$  = stress due to distributed load,  $\sigma_{z_{max}} = \sigma_{z_s} + \sigma_{z_b}$ ,  $\sigma_{z_s}$  = stress due to shrink fitting,  $\sigma_{z_b}$  = stress due to distributed load).

and steel solid shaft are connected by shrink fitting at both ends. Although detail dimensions are different from the ones in Fig. 1(c), the results are useful in this study. Here,  $\sigma_{\theta_s}$  is the shrink fitting stress and  $\sigma_{\theta_{max}} = \sigma_{\theta_s} + \sigma_{\theta_b}$  is the maximum stress when the distributed load  $w=100$  N/mm is applied after shrink fitting. Therefore,  $\sigma_{\theta_b}$  is the stress due to distributed load.

**Figure 2** illustrates the effects of shrink fitting ratio  $\delta/d$  upon stresses  $\sigma_{\theta_s}$ ,  $\sigma_{\theta_{max}}$ ,  $\sigma_{\theta_b}$  and  $\sigma_{z_s}$ ,  $\sigma_{z_{max}}$ ,  $\sigma_{z_b}$ .<sup>13)</sup> In Fig. 2, maximum stresses  $\sigma_{\theta_s}$  and  $\sigma_{\theta_b}$  are indicated at the position where the maximum stress appears. In this figure, fitted length  $L=210$  mm with outer diameter of shaft  $d=210$  mm is considered. Figure 2(a) shows stresses  $\sigma_{\theta_s}$ ,  $\sigma_{\theta_{max}} (= \sigma_{\theta_s} + \sigma_{\theta_b})$  vs.  $\delta/d$  relationship when load distribution  $w=100$  N/mm is applied after shrink fitting. Figure 2(a) also shows stresses  $\sigma_{z_s}$ ,  $\sigma_{z_{max}} (= \sigma_{z_s} + \sigma_{z_b})$  vs.  $\delta/d$  relationship when load distribution  $w=100$  N/mm is applied after shrink fitting. To clarify the effect of distributed load, Fig. 2(b) shows the  $\sigma_{\theta_b} = \sigma_{\theta_{max}} - \sigma_{\theta_s}$  vs.  $\delta/d$  relationship when the load distribution  $w=100$  N/mm is applied. Although stress  $\sigma_{z_b}$  is larger than stress  $\sigma_{\theta_b}$ , stress  $\sigma_{\theta_{max}} (= \sigma_{\theta_s} + \sigma_{\theta_b})$  is

larger than stress  $\sigma_{z_{max}} (= \sigma_{z_s} + \sigma_{z_b})$ . From Fig. 2(b) it is found that  $\sigma_{\theta_{max}}$  has a minimum value at  $\delta/d = 0.50 \times 10^{-4}$ . When  $\delta/d \geq 1.50 \times 10^{-4}$ ,  $\sigma_{\theta_s}$  increases linearly with increasing  $\delta/d$ . On the other hand,  $\sigma_{\theta_b}$  decreases with increasing  $\delta/d$ , and becomes constant when  $\delta/d \geq 1.50 \times 10^{-4}$ . Detail investigations reveal that constant value  $\sigma_{\theta_b} = 10.5$  MPa coincides with the value when the shaft and sleeve are perfectly bonded as a unit body. From Fig. 2(b), it is found that large  $\delta/d$  reduces contact stress  $\sigma_{\theta_b}$  by gripping the shaft tightly. It may be concluded that  $\sigma_{\theta_{max}} = \sigma_{\theta_s} + \sigma_{\theta_b}$  has a minimum value at a certain value of  $\delta/d$ . This is because with increasing  $\delta/d$  stress  $\sigma_{\theta_s}$  increases monotonously but  $\sigma_{\theta_b}$  decreases and becomes constant when  $\delta/d \geq 1.50 \times 10^{-4}$  for  $L=210$  mm. In Ref. 13), the effects of fitted length  $L$  on  $\sigma_{\theta_{max}}$  and  $\sigma_{\theta_b}$  were also considered. Then, it is found that  $\sigma_{\theta_b}$  becomes constant when  $\delta/d \geq 1.50 \times 10^{-4}$  for  $L=100$  mm,  $L=150$  mm, and  $L=210$  mm. Figure 2(b) also indicates  $\sigma_z^{center} = 40$  MPa appearing at the center of the roll where the maximum bending moment is applied. It is seen that  $\sigma_z^{center} = 40$  MPa is nearly equal to  $\sigma_{z_b} = 39.35$  MPa| $\delta/d=0$  and  $\sigma_{\theta_b} = 43$  MPa| $\delta/d=0$ . It should be noted that  $\sigma_z^{center}$  is a reverse stress, and during

the roller rotation  $\sigma_z^{center}=40$  MPa is smaller than the fatigue strength  $\sigma_w=200$  MPa.<sup>15,16)</sup>

In the previous study [13], shrink fitting stress and mechanical stress were considered. Next, thermal stress should be considered. In Fig. 1(c) all ceramic sleeve has high thermal resistance and wear resistance. The steel shaft is usually made of chromium molybdenum steel JIS SCM415, stainless steel JIS SUS304, or high chrome steel JIS STBA26. Since the thermal expansion coefficient of such steel is about four times larger than the one of ceramic, care should be taken for the risk of fracture due to the hoop stress appearing at the ceramic sleeve. **Figure 3** shows 0.2% proof stress  $\sigma_{0.2}$  depending on temperature for SCM415, SUS304, and STBA26.

To consider thermal stress approximately, a simple double cylinder roller consisting of outer ceramic and inner steel SCM415 is considered as shown in **Fig. 4**. **Table 1** shows material properties of the roller used in the analysis. Then, the effect of the inner cylinder thickness on thermal stress  $\sigma_\theta$  appearing at the outer cylinder will be investigated. The results may be obtained theoretically, but here they are obtained in a similar way in Ref. 17). The shrink fitting ratio between ceramics outer cylinder and steel inner cylinder is defined as  $\delta/d$ , where  $\delta$  is the diameter difference and  $d$  is the dimension of the inner diameter of the outer cylinder.

Here,  $\delta/d=2.0 \times 10^{-4}$  is used for investigation, which is only about one fifth of the steel structures. In our previous study, if shrink fitting ratio  $\delta/d$  is larger than  $\delta/d=1.5 \times 10^{-4}$ , the shaft and sleeve can be treated as a unit body when thermal and mechanical stresses are considered.<sup>13)</sup> Heating time is assumed as 0–5 000 s. The heating is applied on the outside surface of the outer cylinder, while the air cooling is applied on the inside surface of the inner cylinder in double cylinder

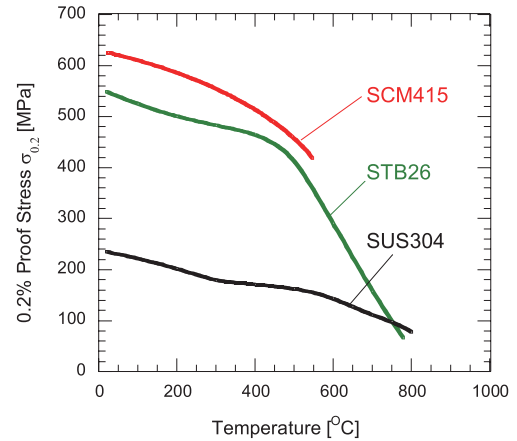


**Fig. 3.** The 0.2% Proof stress  $\sigma_{0.2}$  vs. temperature for SCM415, SUS304, and STB26. (Online version in color.)

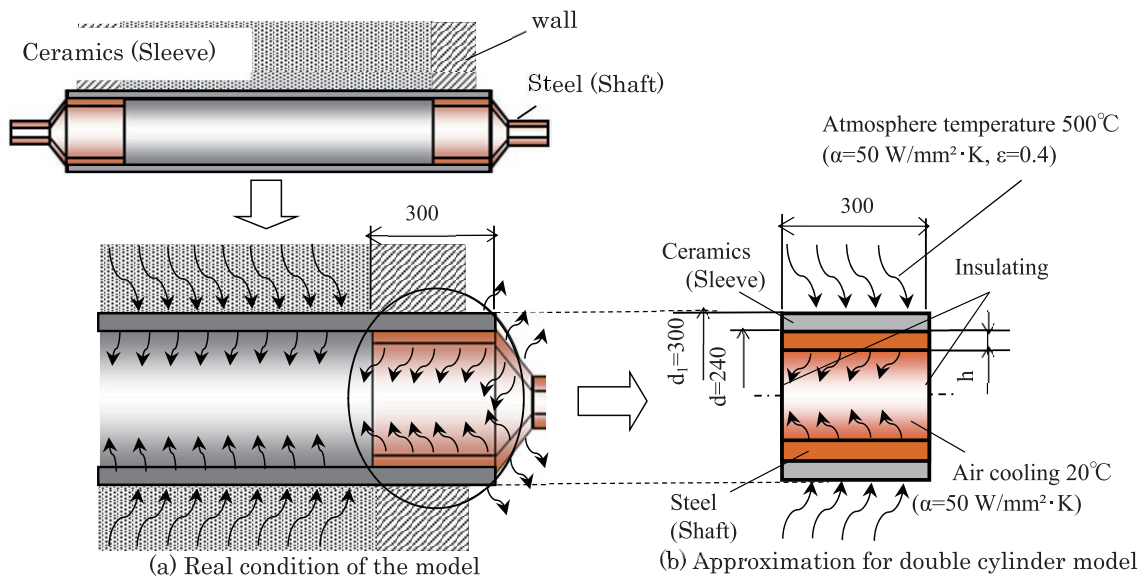


**Fig. 4.** Thermal boundary condition on double cylinder model (a) Real condition of the model, (b) Approximation for double cylinder model. (Online version in color.)

**Table 1.** Properties of material of the proposed rollers at room temperature.

Properties of Material	Ceramics	JIS SCM415	JIS SUS304	JIS STB26
Young's modulus [GPa]	300	210	200	210
Poisson's ratio	0.28	0.3	0.3	0.3
Mass density [kg/m <sup>3</sup> ]	3 300	7 800	7 930	7 550
Thermal conductivity [W/m·K]	62.5	25	14.5	45
Thermal expansion coefficient [1/K]	$0.28 \times 10^{-5}$	$1.2 \times 10^{-5}$	$1.68 \times 10^{-5}$	$1.15 \times 10^{-5}$
Specific heat [J/kg·K]	650	477	480	461
Allowable stress as 0.2%Proof stress [MPa]	333	600	235	549

roller. The connected part in Fig. 4(a) is located at the wall of the furnace whose temperature is assumed about 500°C in Fig. 4(b), which is close to the average temperature between wall temperature inside and room temperature outside in Fig. 4(a). Since the thermal expansion coefficient of the steel is about four times larger than the one of the ceramic, the inner cylinder tends to expand more. The contact heat transfer coefficient is assumed as  $1.0 \times 10^9 \text{ W/m}^2\cdot\text{K}$ . Heat conduction analysis is performed by using the mesh similar to Fig. 8 shown later.

Figure 5 shows stress  $\sigma_\theta$  appearing at the inside surface of the outer cylinder. Here, maximum thermal stress  $\sigma_\theta$  is indicated with varying the thickness  $h$  of inner cylinder. It should be noted that smaller thickness  $h$  has smaller thermal stress  $\sigma_\theta$  because of the smaller rigidity of inner cylinder. For example, when  $h=30 \text{ mm}$  is changed to  $h=10 \text{ mm}$ , the maximum stress becomes less than allowable stress of ceramic  $\sigma_{al}=333 \text{ MPa}$ <sup>18,19)</sup> with safety factor of 1.5.

It should be noted that usually thicker structures are safer than thinner ones, but Fig. 5 shows that thinner ceramic/steel structures are safer than thicker ones.

### 3. Thermal Stress Can be Reduced by Applying Tapered Shaft

#### 3.1. Boundary Conditions

In this study, ceramics roller used in the furnace will be investigated under temperature 1 200°C. The previous chapter indicates that the smaller inner thickness produces smaller  $\sigma_\theta$  at the outer cylinder. However, the extremely small thickness may be unsuitable for the bending load. For example, in Fig. 5,  $h=30 \text{ mm}$  provides  $\sigma_\theta=670 \text{ MPa}$  which is too large compared to allowable stress  $\sigma_{al}=333 \text{ MPa}$ , and  $h=10 \text{ mm}$  looks quite small. Therefore, we assume  $h=20 \text{ mm}$  to be used for the real roller in the first place. Figure 6 shows dimensions of the roller with  $h=20 \text{ mm}$ . Considering of the previous study, Fig. 6 has the shrink fitting ratio  $\delta/d=2.0 \times 10^{-4}$  and fitted length ratio  $L/d=1.22$ .

Figure 7 shows thermal and mechanical boundary conditions on the roller. As shown in Fig. 7(a), the heating is applied on the outside surface of the sleeve with temperature

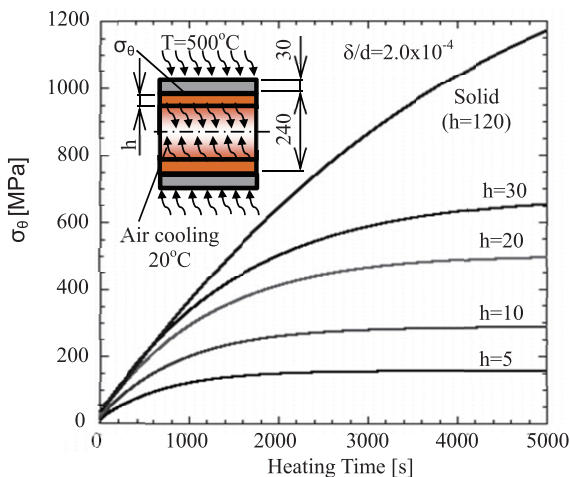


Fig. 5.  $\sigma_\theta$  at the inside surface of the outer cylinder vs. time with varying the thickness of the inner cylinder  $h$ . (Online version in color.)

1 200°C, while air circulation is applied on the inside surface of roller. Here the roller consists of a ceramics sleeve and two steel shafts connected by shrink fitting with ratio  $\delta/d=2.0 \times 10^{-4}$ , which is only about one fifth of the steel structures.<sup>13)</sup> The inside of the roller is cooled by air instead

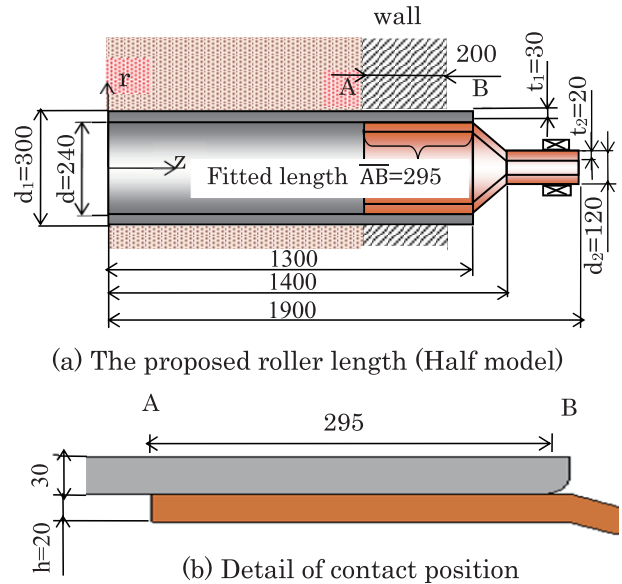


Fig. 6. Dimensions of the proposed roller with shrink fitting ratio  $\delta/d=2.0 \times 10^{-4}$  (a) The proposed roller length (Half model), (b) Detail of contact position. (Online version in color.)

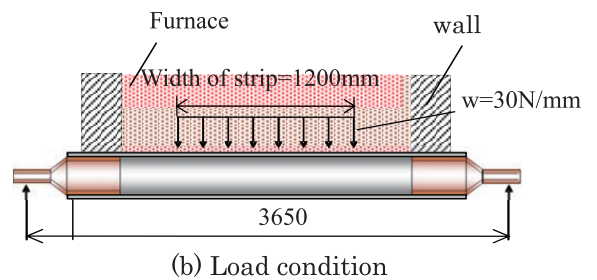
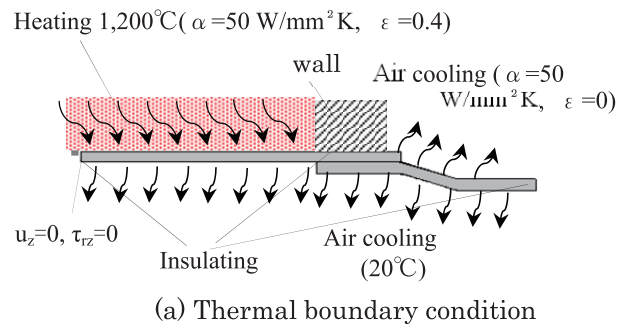


Fig. 7. Boundary condition (a) Thermal boundary condition, (b) Load condition. (Online version in color.)

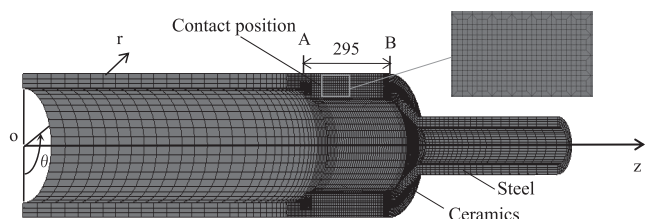


Fig. 8. Three dimensional FEM model (Similar mesh is used for double cylinder model).

of water used for conventional roller. The air temperature is approximately 20°C, and the roller is subjected to distributed load  $w=30\text{ N/mm}$  as shown in Fig. 7(b). Table 1 represents the material properties of the roller where the sleeve is silicon nitride and the shaft is SCM415. Tensile strength of ceramics 500 MPa in Table 1 is estimated as the half value of the bending strength 1 000 MPa.<sup>18,19)</sup> Figure 8 shows the finite element mesh where the 1/4 model is considered due to symmetry. The same mesh is used for heat conduction and thermal stress analyses. Static structural analysis is performed to the models by using MSC. Marc Mentat2011 with full Newton-Raphson iterative sparse solver of multifrontal method. The total number of elements is 25780 and the total number of the nodes of 31626.

**3.2. Analysis of Joint Structure of the Roller**

Here, stress appearing on the ceramic sleeve is discussed under atmosphere temperature 1 200°C. Figure 9 shows temperature variation on the outer surface of the ceramic sleeve vs. time. It is seen that a steady temperature for all points appears after heating time 6 000 s. Figure 9 shows the steady temperatures at points a-e, that is,  $T_a=T_b=1\ 076^\circ\text{C}$ ,  $T_c=835^\circ\text{C}$ ,  $T_d=490^\circ\text{C}$ , and  $T_e=297^\circ\text{C}$ . In the previous chapter, the atmosphere temperature was assumed as 500°C, which is close to the temperature at point d. Therefore, we have confirmed that the assumed double cylinder model is

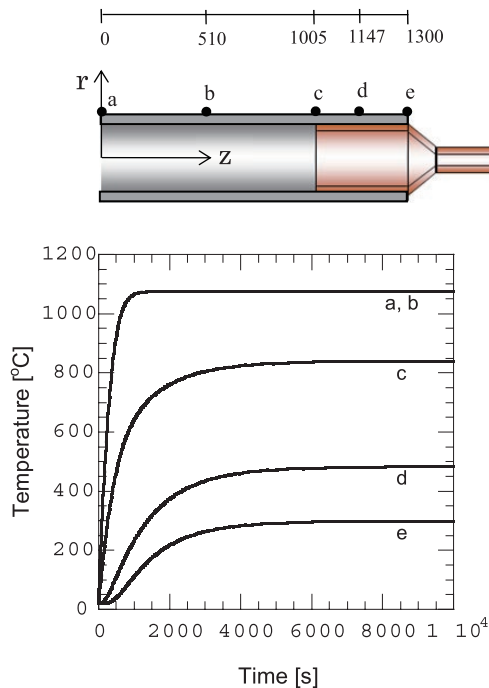


Fig. 9. Temperature on the outer surface of the sleeve (point a, b, c, d, and e) vs. time. (Online version in color.)

valid.

In this study, three types of shaft models will be analyzed and the strength will be discussed. Table 2 and Fig. 10 show the three models, namely, the uniform thickness of shaft model (Model 1), the tapered shaft model (Model 2), and the short tapered shaft model (Model 3). Table 2 represents the detail dimensions of those models.

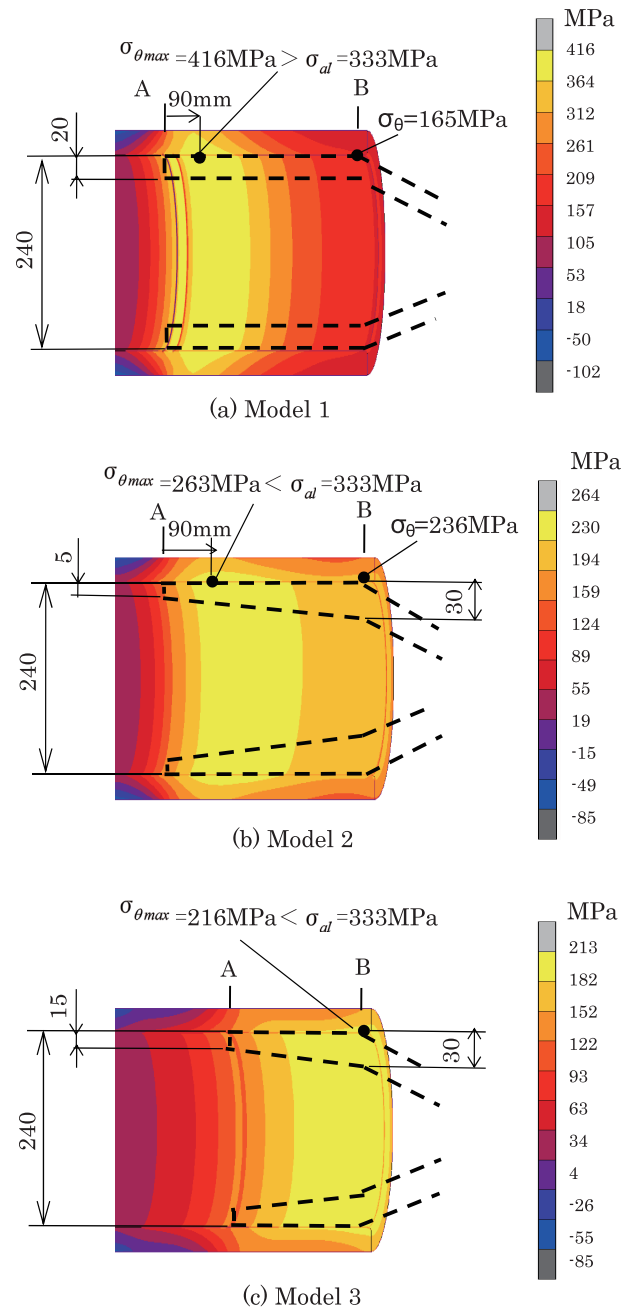


Fig. 10. Thermal stress  $\sigma_{\theta\max}$  for ceramics sleeve with (a) Model 1, (b) Model 2, (c) Model 3. (Online version in color.)

Table 2. Thickness of structural joint of the roller for each model (see Fig. 9).

	Sleeve Thickness [mm]	Shaft Thickness [mm]	Fitted Length [mm]	Outer Diameter of the Shaft [mm]	Ratio Fitted Length (L/d)	Shape of The Shaft
Model 1 (standard)	30	20	295	240	1.22	Uniform
Model 2	30	5–30	295	240	1.22	Taper
Model 3	30	15–30	180	240	0.75	Short and taper



### 3.3. The Maximum Tensile Stress of the Ceramic Sleeve

Figure 10 shows stress distributions  $\sigma_\theta$  for ceramic sleeve under heating load temperature 1200°C. As can be seen in Fig. 10, the maximum stresses appear as  $\sigma_{\theta\max}=416$  MPa  $>$   $\sigma_{al}$  for Model 1,  $\sigma_{\theta\max}=263$  MPa  $<$   $\sigma_{al}$  for Model 2, and  $\sigma_{\theta\max}=216$  MPa  $<$   $\sigma_{al}$  for Model 3. By applying tapered model, the maximum stress decreases by 37% for Model 2 and by 50% for Model 3. Maximum stress  $\sigma_{\theta\max}$  for Model 1 is higher than the tensile strength, while  $\sigma_{\theta\max}$  for Model 2 and 3 are lower. This is because the rigidity of shaft for Model 1 is the largest among the models.

### 3.4. Strength Analysis of the Steel Shaft Based on Plastic Deformation

Figure 11 illustrates hoop stress  $\sigma_\theta(z)$ , Mises equivalent stress  $\sigma_{eq}(z)$  and temperature distributions  $T(z)$  along the contact position of the shaft. In Fig. 11,  $\sigma_\theta(z)$  and  $\sigma_{eq}(z)$  are compared with proof stress  $\sigma_{0.2}(z)$  for SCM415,<sup>20</sup> which is depending on  $T(z)$ . It is seen that temperature  $T(z)$  decreases from  $z=0$  to  $z=300$  mm. Stresses  $\sigma_\theta(z)$  and  $\sigma_{eq}(z)$  along the contact surface decrease with decreasing temperature  $T(z)$  in a similar way. On the other hand, 0.2% proof stress  $\sigma_{0.2}(z)$  of material SCM415 increases with decreasing the temperature  $T(z)$ . Here, proof stress  $\sigma_{0.2}(z)$  is regarded as the allowable stress of the steel shaft. Since plastic deformation is not desirable, stress  $\sigma_\theta(z)$  should be lower than 0.2% proof stress  $\sigma_{0.2}(z)$  at the shaft temperature  $T(z)$ , that is  $|\sigma_\theta(z)| < |\sigma_{0.2}(z)|$ . In Fig. 11, the region where  $|\sigma_\theta(z)| > |\sigma_{0.2}(z)|$  is a critical region because plastic deformation occurs. While the other region where  $|\sigma_\theta(z)| < |\sigma_{0.2}(z)|$  is a safe region because plastic deformation does not occur. It is seen that Model 1 and Model 2 have plastic deformation, and only Model 3 is elastic. Consequently, it is found that the short tapered shaft model (Model 3) is the most desirable. Here,  $\sigma_\theta(z)$  and  $\sigma_{0.2}(z)$  are compared conveniently although more accurately,  $\sigma_{eq}(z)$  and  $\sigma_{0.2}(z)$  should be compared. As shown in Fig. 11, the difference between  $\sigma_\theta(z)$  and  $\sigma_{eq}(z)$  is within 34%. It should be noted that if  $|\sigma_\theta(z)| < |\sigma_{0.2}(z)|$  is satisfied,  $|\sigma_{eq}(z)| < |\sigma_{0.2}(z)|$  is guaranteed.

In this study, thermal stress is mainly considered because FEM analysis shows that the effect of distributed load  $w$  is less than 2% compared to the one of thermal stress. For example, in Fig. 12 shown in the next section, stress amplitude  $\sigma_{\theta a}$  is only a few percent of average stress  $\sigma_{\theta ave}$ . Stress  $\sigma_{\theta a}$  appears due to distributed load  $w$  and average stress  $\sigma_{\theta ave}$  appears due to thermal stress and shrink fitting. Therefore, Fig. 12 shows that the effect of distributed load  $w$  is very small.

### 3.5. Fatigue Strength for Ceramic Sleeve

In this study, fatigue strength is considered when the roller is rotating under distributed load. The fatigue problem due to stress fluctuation can be examined by using stress amplitude  $\sigma_{\theta a}$  and average stress  $\sigma_{\theta ave}$ , which is defined by the following equation.

$$\sigma_{\theta ave:A,B} = \frac{\sigma_{\theta\max:A,B} + \sigma_{\theta\min:A,B}}{2} \quad \sigma_{\theta a:A,B} = \frac{\sigma_{\theta\max:A,B} - \sigma_{\theta\min:A,B}}{2} \quad \dots (1)$$

The results obtained by Eq. (1) at point A and B are plotted in the endurance limit diagram as shown in Fig. 12. Figure 12 shows the results at point A and point B where

the maximum stress  $\sigma_{\theta\max A}$  and  $\sigma_{\theta\max B}$  appear. Here, point A has the maximum tensile stress, while point B has the highest stress amplitude stress. Tensile strength  $\sigma_{al}=333$

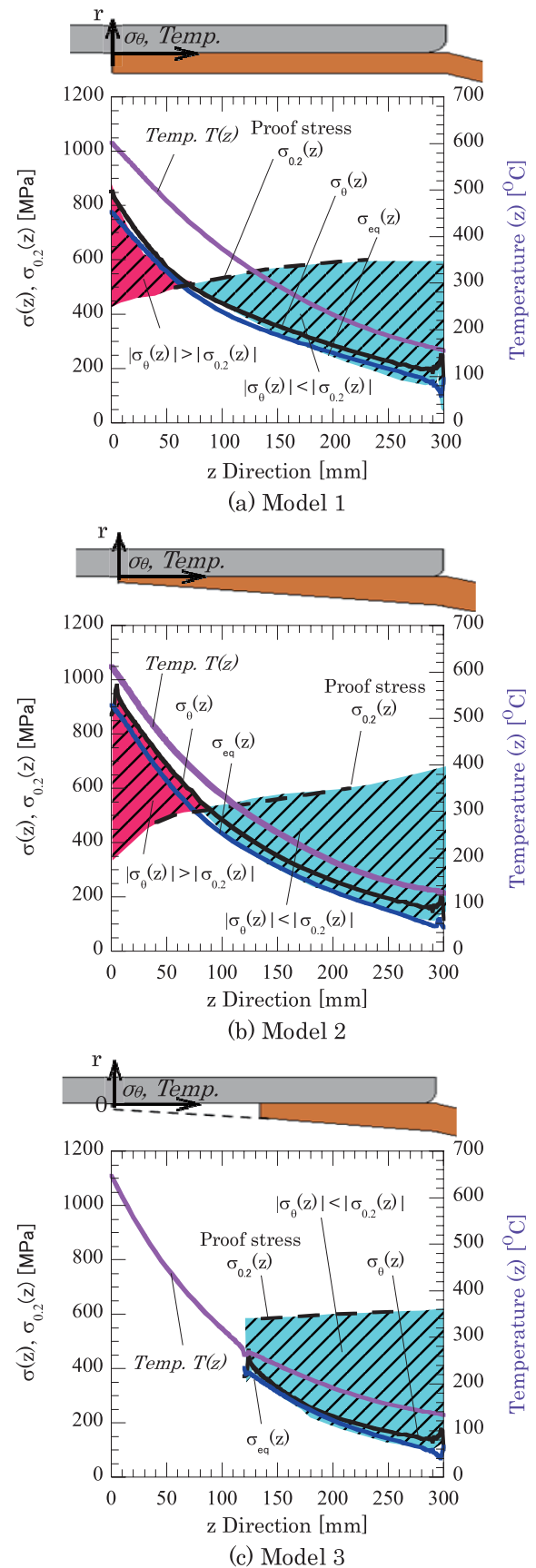


Fig. 11. Stress and temperature distribution along contact position of shaft toward the 0.2% proof stress (a) Model 1, (b) Model 2 (c) Model 3. (Online version in color.)

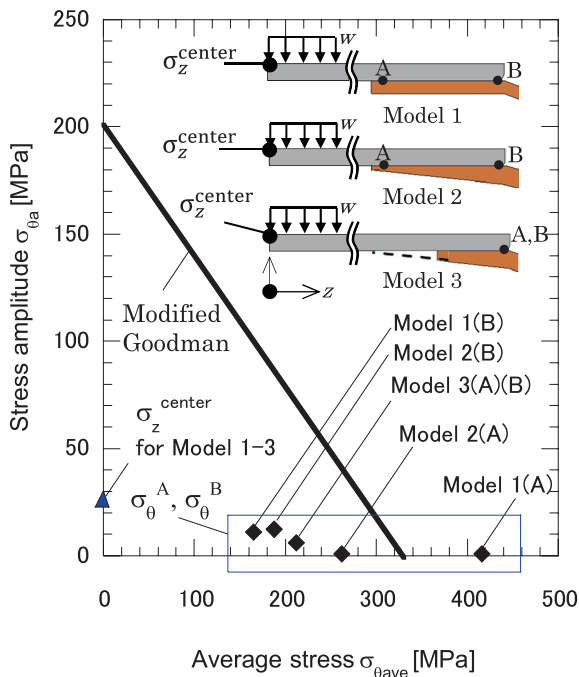


Fig. 12. Endurance limits of ceramic sleeve. (Online version in color.)

MPa<sup>18,19</sup>) is plotted on the vertical axis, while fatigue limit  $\sigma_w=200$  MPa<sup>15,16</sup>) is plotted on the horizontal axis. Figure 12 also shows bending stress  $\sigma_z^{center}$  at the center of the roll, which has the same value for Model 1~ Model 3. It is seen that  $\sigma_z^{center}=22.86$  MPa  $<$   $\sigma_w=200$  MPa.

First we consider the maximum average stress  $\sigma_{\theta ave}$  at point A in Fig. 12. The maximum values are  $\sigma_{\theta ave}=210$ – $420$  MPa. The average stress for Model 1 is  $\sigma_{\theta ave}=420$  MPa, which is larger than the value of fatigue limit  $\sigma_{al}=333$  MPa. However, the stress amplitudes at point A for Model 1 and 2 is almost zero  $\sigma_{\theta A}\approx 0$ , and for Model 3  $\sigma_{\theta A}=5$  MPa. It is seen that the results for Model 2 and Model 3 are below the durability line of the ceramics material.

Next, we consider maximum stress amplitude  $\sigma_{\theta A}$  at point B in Fig. 12. Stress amplitude  $\sigma_{\theta A}$  for Model 1 and 2 is about  $\sigma_{\theta A}=10$  MPa, and for model 3 is about  $\sigma_{\theta A}=5$  MPa. From Fig. 12, it is found that the results for Model 1, 2, and 3 are below the durability line of ceramic material. According to both Fig. 12, the fatigue failure does not occur although Model 1 has large average stress.

#### 4. Application of Ceramic/steel Rollers to a Real Furnace in a Steel Manufacturing Company

##### 4.1. Models Considered

In the previous chapters, a ceramic roller consisting of a ceramic sleeve and steel shafts was considered. In this chapter, an application of ceramic roller to a real furnace in a steel manufacturing company is considered. The company suggests that the roller should consist of three pieces, namely, main-sleeve, intermediate-sleeve, and shaft. The advantage of this three pieces structure is that the damaged components can be changed with low cost. The three components are assumed to be connected by shrink fitting with the ratio  $\delta/d=2.0\times 10^{-4}$ .<sup>13)</sup>

Figure 13 shows dimensions of the stainless steel roller

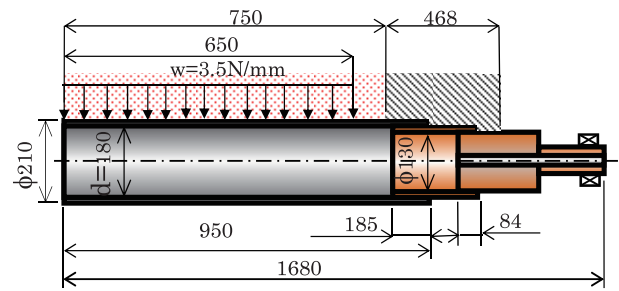


Fig. 13. Dimensions of the roller considered in the company A. (Online version in color.)

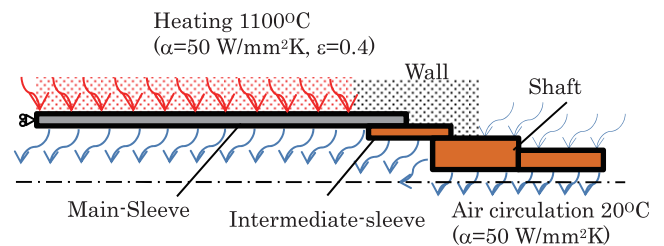


Fig. 14. Boundary conditions of the real ceramics roller. (Online version in color.)

Table 3. Comparison of materials.

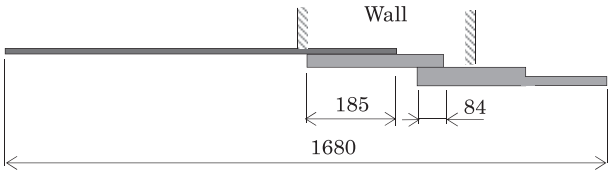
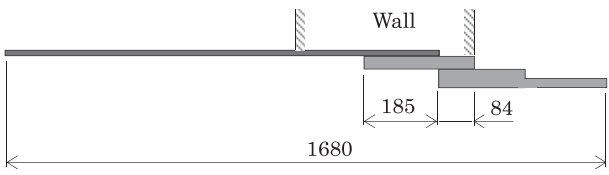
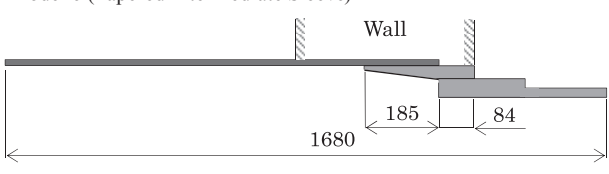
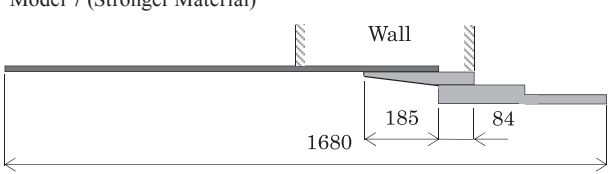
Items	SCM415	SUS304	STB26
Economical?	yes	no	no
High Strength under high temperature?	yes under 550°C	no	yes
High Oxidation resistance under high temperature?	no	yes	yes

used in a steel company. The length of the half roller is 1 680 mm with outer diameter of 210 mm, and thickness of the wall is 468 mm. The wall is assumed to be insulated. In the first place, by using the dimension in Fig. 13, the main-sleeve material is changed to ceramic and also the water cooling is changed to air cooling at the same time. This model is named Model 4. Figure 14 shows the boundary conditions of the air cooling. The heating is applied on the outside surface of the ceramic sleeve with temperature 1 100°C. Also, the air cooling 20°C is applied on the inside surface of the roller.

Since the company has used all stainless steel rollers, in the first place, SUS304 is assumed as the intermediate-sleeve and shaft material because of economy. Since the strength of SUS304 is low as shown in Fig. 3, other materials are also considered. Table 3 shows comparison between SCM415, SUS304, and STB26. It is noted that the material SCM415 considered in the previous section cannot be used here because of low oxidation resistance under high temperature.

Table 4 shows dimensions and materials four types of models. Model 4 is a basic model first we consider as described above. For Model 5, the joint position is shifted away from the core furnace in order to avoid high temperature effects although the total length of the roller 1 680 mm is the same as the length of Model 1. For Model 6, a tapered intermediate-sleeve is considered to reduce the stress on the main-sleeve. The last model, Model 7, material of the intermediate-sleeve and shaft are changed from stainless

**Table 4.** Four types of model for real application.

Model	Main Sleeve	Material Intermediate Sleeve	Shaft
Model 4 (Basic) 	Ceramics	JIS SUS304 (18Ni-8Cr)	JIS SUS304 (18Ni-8Cr)
Model 5 (Shifted Joint Parts) 	Ceramics	JIS SUS304 (18Ni-8Cr)	JIS SUS304 (18Ni-8Cr)
Model 6 (Tapered Intermediate Sleeve) 	Ceramics	JIS SUS304 (18Ni-8Cr)	JIS SUS304 (18Ni-8Cr)
Model 7 (Stronger Material) 	Ceramics	JIS STBA26 (9Cr-1Mo)	JIS STBA26 (9Cr-1Mo)

**Table 5.** Maximum stress for all real models application.

Model	Main-Sleeve/Intermediate-Sleeve Joints				Intermediate-Sleeve/Shaft-Joints			
	Main-Sleeve		Intermediate-sleeve		Intermediate-Sleeve		Shaft	
	$\sigma_{\theta_{\max}}$ [MPa]		$\sigma_{\theta_{\max}}$ [MPa]		$\sigma_{\theta_{\max}}$ [MPa]		$\sigma_{\theta_{\max}}$ [MPa]	
Model 4	954	×	-1 007	×	Separated	×	Separated	×
Model 5	376	×	-422	×	-74	✓	-123	✓
Model 6	318	✓	-450	×	-79	✓	-123	✓
Model 7	204	✓	-289	✓	-59	✓	-101	✓

× : dangerous, ✓ : safe

steel JIS SUS304 to high chrome steel JIS STBA26.

Table 1 provides properties of each material at room temperature. Allowable stress of ceramic material  $\sigma_{al}=333$  MPa, while 0.2% proof stress  $\sigma_{0.2}$  for stainless steel JIS SUS304 is  $\sigma_{0.2}=235$  MPa and for high chrome steel JIS STBA26 is  $\sigma_{0.2}=549$  MPa.

#### 4.2. High Chrome Steel Tapered Model Can be Used in a Real Furnace

Table 5 shows the maximum stress appearing at three components. It is seen that the maximum stresses at the main-sleeve/intermediate-sleeve joint are always larger than the ones at intermediate-sleeve/shaft joint. This is because the main-sleeve and the intermediate-sleeve have different thermal expansion coefficients as well as the joint position is close to the core furnace.

From Table 5, Model 4 is unsuitable to be used in the furnace because  $\sigma_{\theta_{\max}}=954$  MPa appears at the main-sleeve, and  $\sigma_{\theta_{\max}}=-1\ 007$  MPa appears at the intermediate-sleeve. Also, it should be noted that the intermediate-sleeve/shaft joint is separated during heating.<sup>17)</sup> By shifting joint portion in Model 5, the maximum stress on the main-sleeve/intermediate-sleeve contact part significantly decreases. However, maximum stress at ceramic sleeve  $\sigma_{\theta_{\max}}=376$  MPa is still larger than allowable stress  $\sigma_{al}=333$  MPa although the intermediate-sleeve/shaft joint is not separated.

In Model 6, to reduce the maximum stress at the ceramic main-sleeve, the tapered intermediate-sleeve model is applied. Table 5 shows that maximum stress at ceramic sleeve  $\sigma_{\theta_{\max}}=318$  MPa is lower than allowable stress  $\sigma_{al}=333$  MPa. However, maximum compressive stress on the intermediate-sleeve  $\sigma_{\theta_{\max}}=450$  MPa is still larger than



the 0.2% proof stress  $\sigma_{0.2}=220$  MPa. For Model 7, the material is changed from the stainless steel JIS SUS304 to the high chrome steel JIS STBA26. Since the thermal expansion coefficient of STB26 is lower than JIS SUS304, maximum compressive stress  $\sigma_{\theta\max}=204$  MPa becomes smaller, and therefore, Model 7 may be the most suitable.

## 5. Failure Analysis for Coming Out of the Shaft From the Ceramic Sleeve

In the previous discussion thermal and mechanical stresses were considered to prevent fracture of the ceramic sleeve, and also stress for the steel shaft was compared to the allowable stress. However, it should be noted that only low shrink fitting ratio can be applied for those structures because of the ceramic brittleness. Actually, coming out of the shaft was sometimes observed in prototype ceramics rolls. Since sliding bearings for rolls and rollers do not restrict the axial movement of the shaft, the coming out can be problematic. Even when the shaft movement is restricted within a small allowable range, the coming out of the shaft may cause local thrust loading, frictional heat generation, and wear preventing smooth rotation of the roller. Although several studies are available for contact failure regarding the shrink fitting assembly for a gear hub and shaft<sup>21)</sup> and for rotating thermos-elastoplastic,<sup>22)</sup> few failure studies are reported for the sleeve and shaft. In this paper, therefore, the coming out behavior of the steel shaft from the ceramics sleeve will be considered during operation.<sup>23,24)</sup>

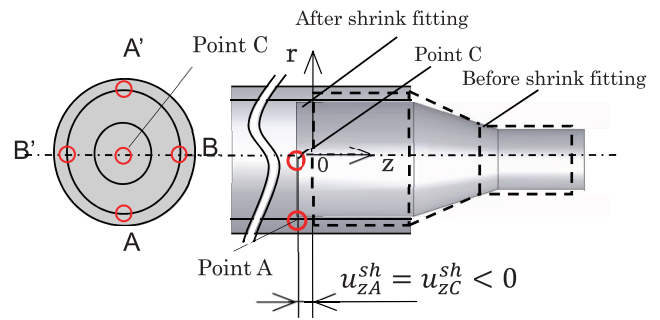
### 5.1. Evaluation for the Coming Out and Deformation of the Shaft

In order to consider coming out behavior, the shaft deformation due to shrink fitting is investigated in the first place. **Figure 15(a)** illustrates the shaft deformation with the  $(r,z)$  coordinate defined before shrink fitting. Displacement  $u_{zC}$  in the  $z$ -direction is determined from the values at 4 points as  $u_{zC}^{sh} = (u_{zA}^{sh} + u_{zA'}^{sh} + u_{zB}^{sh} + u_{zB'}^{sh})/4 = u_{zA}^{sh} < 0$  as shown in Fig. 15(a). Then, since the shaft is under compression in the  $r$ -direction; we have  $u_{zA}^{sh} = u_{zC}^{sh} < 0$ .

On the other hand, Fig. 15(b) shows the shaft due to initial distributed load  $N=0$  focusing on displacement  $u_{zA}^{N=0}$ . As shown in Fig. 15(b), the positive displacement  $u_{zA}^{N=0} (>0 > u_{zA}^{sh})$  appears at point A although the displacement due to shrink fitting was negative  $u_{zA}^{sh} < 0$  as shown in Fig. 15(a). On the other hand, at point C, displacement  $u_{zC}^{N=0} (> u_{zC}^{sh})$  appears but usually still negative  $u_{zC}^{N=0} < 0$ . Those values  $u_{zA}^{N=0}$  and  $u_{zC}^{N=0}$  are defined as the initial displacement at  $N=0$  considering both shrink fitting and initial loading.

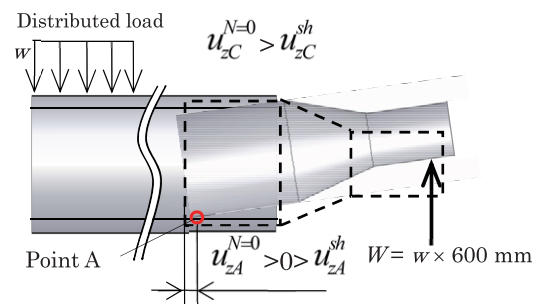
### 5.2. Analysis of the Coming Out of the Shaft for Each Model

**Figure 16** shows displacement  $u_{zC}$  vs. the number of cycle  $N$  for Model 1, Model 2, and Model 3 whose distributed load  $w=30$  N/mm. The magnitude of the load for Model 1–3 is assumed to be the largest one considering several cases in industries. Table 2 shows the shaft geometry for Model 1–3. In Fig. 15, displacement  $u_{zC}$  increases with increasing  $N$  for all models. For Model 1, displacement  $u_{zC}$  increases slightly after  $N=1$ , therefore the coming out may happen. For Model 2, the coming out is easier to



(a) Displacement due to shrink fitting

$$u_{zC}^{sh} = (u_{zA}^{sh} + u_{zA'}^{sh} + u_{zB}^{sh} + u_{zB'}^{sh})/4 = u_{zA}^{sh}$$



(b) Displacement due to shrink fitting and initial load at  $N=0$

**Fig. 15.** Shaft displacement due to shrink fitting and bending load (a) Displacement due to shrink fitting  $u_{zC}^{sh} = (u_{zA}^{sh} + u_{zA'}^{sh} + u_{zB}^{sh} + u_{zB'}^{sh})/4 = u_{zA}^{sh}$  (b) Displacement due to shrink fitting and initial load at  $N=0$ . (Online version in color.)

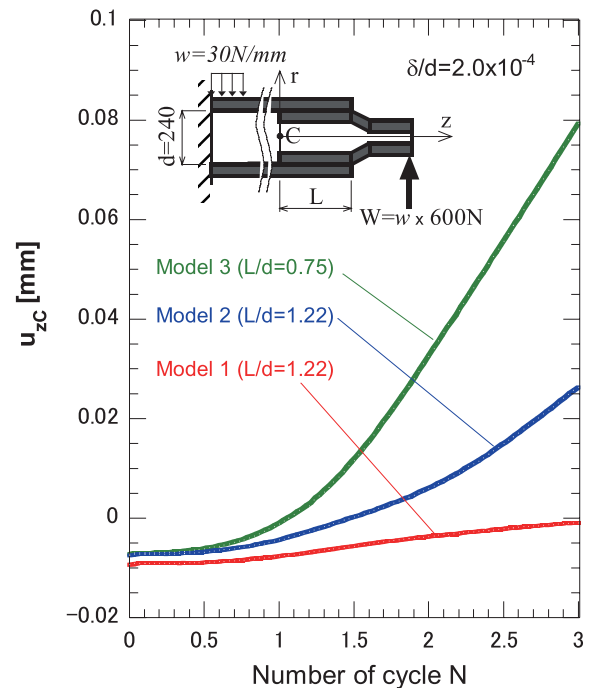


**Fig. 16.** The  $z$ -displacement  $u_{zC}$  of the shaft vs. number of cycle  $N$  for Model 1, 2, and 3. (Online version in color.)

occur than for Model 1 because of smaller shaft thickness. For Model 3, displacement  $u_{zC}$  increases significantly with increasing  $N$  because Model 3 has smaller contact length as well as smaller shaft thickness. From Fig. 16, displacement  $u_{zC}$  increases largely when smaller contact length and

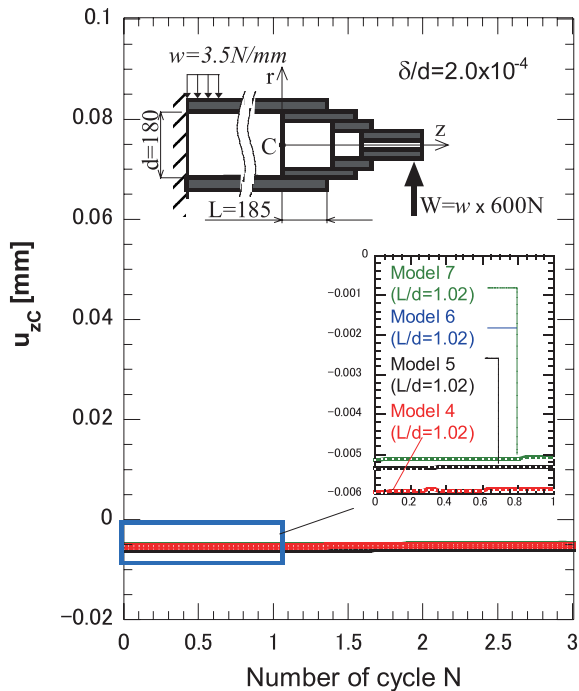


Fig. 17. The z-displacement  $u_{zc}$  of the shaft vs. number of cycle N for Model 4, 5, 6 and 7. (Online version in color.)

smaller thickness of the shaft. The smaller contact length has smaller friction force and the smaller thickness has smaller rigidity.

Figure 17 shows the coming out for real roller whose load  $w=3.5$  N/mm in Fig. 13. The load is about 9 times smaller than the one of Fig. 1(c). Figure 17 shows the coming out for Model 4–7. Displacement  $u_{zc}$  is much smaller than one of Fig. 16. It may be concluded that the coming out of the shaft does not occur in the real roller applications. In the other words, the magnitude of the load considered in Fig. 7(b) is too large because we assume the most dangerous case when we consider the ceramics roller applications.

## 6. Conclusions

Developing advanced ceramic structure has been promoted in USA, Japan, and Germany since 1970s. Although most of the projects did not succeed substantially, large ceramic rolls and rollers are recently used at steel manufacturing machinery successfully. To promote those large cylindrical ceramic, this paper considered the heath roller consisting of ceramics sleeve and steel shaft connected by shrink fitting. Since the thermal expansion of the steel shaft is larger than the one of the ceramic sleeve, the ceramic sleeve is subjected to large hoop stress at the contact portion. As a result of the joint structure analysis, the conclusions can be summarized in the following way.

(1) Simple double cylinder model shows that the maximum stress can be reduced by using the small thickness of

the steel shaft.

(2) Finite element analysis shows that the maximum tensile stress can be reduced by using tapered thickness shaft because of the smaller rigidity at the high temperature portion. It is also found that the plastic deformation of the shaft does not appear by applying the short tapered shaft geometry on the structure.

(3) An application of ceramic roller to a real furnace in a steel manufacturing company is considered. It is found that tapered shaft geometry with high chrome steel can be used in a real furnace.

(4) Failure analysis for coming out of the shaft is also considered in this study. The results show that the coming out does not happen in the real rollers because of the small displacement of the shaft.

## REFERENCES

- 1) R. P. Larsen and A. D. Vyas: The Outlook for Ceramics in Heat Engines: 1900-2010, SAE Paper No. 880514, Society of Automotive Engineers, Dearborn, MI, (1998).
- 2) P. Wray: Advanced Structural Ceramics, Tech Monitoring, SRI International, Japan, (1991).
- 3) S. Jahanmir: Friction and Wear of Ceramics, Marcel Dekker, New York, (1994).
- 4) U. Dworak: High-tech Ceramics "Viewpoints and perspectives", ed. by K. Gernot, Academic Press Limited, London, (1989), 1.
- 5) F. Bonollo, J. R. Urban, B. Bonatto and M. Botter: *Alluminio E Leghe*, **6** (2005), 23.
- 6) N. A. Noda, Hendra, Y. Takase and W. Li: *J. Solid Mech. Mater. Eng.*, **3** (2009), 1090.
- 7) N. A. Noda, Hendra, W. Li and Y. Takase: *Trans. Jpn. Soc. Mech. Eng.*, **4** (2010), 1198.
- 8) M. J. Ryan, R. Young, D. Manning, G. V. White, I. W. M. Brown, C. Yu Chen and R. Stanley: *J. Am. Chem. Soc.*, **49** (2013), 44.
- 9) E. Ogawa, S. Hamayoshi, M. Kumagai, K. Shimizu, N. A. Noda, Y. Takase, K. Kishi, K. Shobu, T. Tabaru, E. Maeda, S. Kago and T. Matsuda: Proc. 8th Int. Conf. on Zinc and Zinc Alloy Coated Steel Sheet, AIM, Italy, (2011), 1.
- 10) E. Miki: *Plant Eng.*, **21** (1989), 8.
- 11) N. A. Noda, Y. Sano, Y. Takase, W. Li and H. Sakai: *Int. J. Entrepren. Innovat. Manag.*, **1** (2011), 77.
- 12) N. A. Noda, M. Yamada, Y. Sano, S. Sugiyama and S. Kobayashi: *Eng. Fail. Anal.*, **15** (2008), 261.
- 13) N. A. Noda, Hendra, Y. Takase and M. Tsuyunaru: *J. Solid Mech. Mater. Eng.*, **2** (2008), 1410.
- 14) N. Yokoyama, A. Mori, M. Kono and M. Yoshida: Japanese Patent Disclosure No. 2000-249472, (2000).
- 15) I. Sai and S. Horibe: Static Fatigue of Ceramics and Cyclic Fatigue, Extra ed., Metal, Japan, (1993).
- 16) Japan Society of Mechanical Engineers Reviews: Material Design of Metal Fatigue Strength I (General, Size Effect, Notch Effect), 2nd ed., JSME, Japan, (2007).
- 17) W. Li, N. A. Noda, H. Sakai and Y. Takase: *J. Solid Mechanics. Mater. Eng.*, **5** (2011), 14.
- 18) 136th Committee Processing Technology of Japan Society of Promotion and Science: Fine Ceramics Research Handbook, Uchida Roukakuho, Japan, (1998), 414 (in Japanese).
- 19) Ceramics Editorial Committee: Mechanical Properties of Ceramics, 3rd ed., Ceramics Association, Japan, (1982), 65.
- 20) 129th Committee, 3rd Subcommittee of Japan Society of Promotion and Science: Metal Material High-temperature Strength Data Collection, Part 1, Low Alloy Steel Reviews. Yokendo, Japan, (1964), 9 (in Japanese).
- 21) C. E. Truman and J. D. Booker: *Eng. Fail. Anal.*, **14** (2007), 557.
- 22) N. Antoni: *Appl. Math. Mech.*, **37** (2003), 2352.
- 23) N. A. Noda, Y. Sano, Y. Takase, S. Harada, D. Suryadi and S. Kumasaki: *Tetsu-to-Hagané*, **101** (2015), 284.
- 24) N. A. Noda, D. Suryadi, S. Kumasaki, Y. Sano and Y. Takase: *Eng. Fail. Anal.*, **57** (2015), 219.